Deflection of phototactic microswimmers through obstacle arrays

Marvin Brun-Cosme-Bruny,[1,*] Andre Förtsch,[2,*] Walter Zimmermann [2,†] Eric Bertin [1,‡]
Philippe Peyla [1,§] and Salima Rafaï [1,‖]

[1]*Université Grenoble Alpes, CNRS, LIPhy, F-38000 Grenoble, France*
[2]*Theoretische Physik, Universität Bayreuth, D-95447 Bayreuth, Germany*

We study the effect of inhomogeneous environments on the swimming direction of the microalgae *Chlamydomonas reinhardtii* (CR) in the presence of a light stimulus. Positive or negative phototaxis describe the ability of microorganisms to bias their swimming toward or away from a light source. Here we consider microswimmers with negative phototaxis in a microfluidic device with a microfabricated square lattice of pillars as obstacles. We measured a mean deflection of microswimmers that shows an interesting nonlinear dependence on the direction of the guiding light beam with respect to the symmetry axes of the pillar lattice. By simulating a model swimmer in a pillar lattice and analyzing its scattering behavior, we identified the width of the reorientation distribution of swimmers to be also crucial for the nonlinear behavior of the swimmer deflection. On the basis of these results we suggest in addition an analytical model for microswimmers, where the pillar lattice is replaced by an anisotropic scattering medium, that depends only on a scattering rate and the width of the reorientation distribution of swimmers. This flexible and handy model fits the experimental results as well. The presented analysis of the deflection of light guided swimmers through pillar lattice may be used for separating swimmers having different reorientation distributions.

I. INTRODUCTION

Far from any walls, planktonic microorganisms swim freely, while in a complex environment they often adhere or attach on surfaces [1], for example, when bacterial colonies are embedded in biosynthesized extracellular polymeric substances [2,3]. This can lead to the so-called biofouling [4]. In microfluidic devices [5], the same process can occur and leads to a destruction of the device. The way microorganisms move inside and colonize a porous medium such as a membrane or a filter is a subject of current research [6–8]. The statistics of transport of microswimmers through a crowded environment have been explored in recent works [9,10]. Collective patterns like vortices have also been reported for swimming bacteria in arrays of pillars [11].

Can microswimmers be guided through complex environments? Deformable particles such as (red blood) cells or even simple dumbbells driven by a fluid flow through inhomogeneous landscapes show interesting deflection scenarios [12–14]. For instance, particle loaded flows through arrays of pillars are a very important microfluidic technique that enables a continuous

---

[*]These authors contributed equally to this work.

[†]walter.zimmermann@uni-bayreuth.de

[‡]eric.bertin@univ-grenoble-alpes.fr

[§]philippe.peyla@univ-grenoble-alpes.fr

[‖]salima.rafai@univ-grenoble-alpes.fr

size- or deformability dependent particle sorting with exceptional resolution, depending on the relative orientation between the flow direction and a symmetry axis of obstacle arrays [12,14]. In the case of the phototactic microswimmer *Chlamydomonas reinhardtii* (CR), the position of a light source defines instead of the flow a preferred direction [15]. This light orientation of the algae CR is rather effective and leads for instance to self-focusing of microswimmers in Poiseuille flow [16] including interesting jet instabilities [17,18]. Investigations of the interaction of self-propelled particles with a complex environment in general is a challenging current research topic with various applications [19–25].

Here, we investigate negative phototactic motile algae CR moving away from a light source through a microfluidic device with a transparent and regular lattice of microfabricated pillars as described in Sec. II. These motile algae experience by the pillar lattice a deviation between their average swim directions and the light beam, cf. Sec. III. To understand the origin of such deviations, we perform simulations taking only into account collisions between swimmers and pillars and statistical reorientations. By comparing these results with Lattice Boltzmann (LB) simulations that include hydrodynamic interactions (HI), we can extract the role of different key features, as described in Sec. IV.

The numerical simulations can account for our experimental results whereby the intrinsic orientational noise of the swimmers is crucial for a broadening of the distribution of the swim orientation around the light beam. In Sec. V a simple analytical model is developed, which is also closely connected to the numerical analysis. Both approaches cover the essential experimental observations. A discussion of several results and conclusions is given in Sec. VI.

II. EXPERIMENTAL SET-UP

We use as a microswimmer model the green microalga CR, a biflagellate photosynthetic and phototactic cell of 10 μm diameter [26]. The wild type strain CC-124 from the Chlamydomonas Resource Center collection and that is described as negatively phototactic is used. The microalgae are grown under a 14h/10h light/dark cycle at 22 °C and are harvested in the middle of the exponential growth phase. CR's front flagella beat in a breast stroke manner and propel the microswimmer in the fluid [27]. The swimming motion is characterized by a persistent random walk in the absence of a bias [28,29]. However, in the presence of a light stimulus (green wavelength, i.e., around 510 nm), microalgae tend to swim away from the light source [15]. Suspensions are used at an initial volume fraction of about 0.05%, so that the HI among microswimmers is negligible. The cells, homogeneously distributed, are introduced within a chamber containing a square lattice of 200 μm-diameter pillars regularly spaced by a minimal surface-to-surface distance $d = 30 \mu$m. The pillar lattice has been designed such that the length of a unit cell of pillars is comparable to the persistence length of swimmers, to allow for the reorientation of swimmers while passing through it. Pillars are made of transparent PDMS by means of soft lithography processes [30]. Both the diameter and inter-pillar distance are kept constant. The height of pillars is 70 μm corresponding to about 7 cell diameters. Bovine Serum Albumine is used to coat the pillars to limit adsorption of cells. The space surrounding the complex environment is free of pillars.

We observe the cells under a bright field microscope. We use an inverted microscope (Olympus IX71) coupled with a CCD camera (AVT GX3300) used at a frame rate of 15 fps. Using a low magnification objective ($\times 2$) allows us to get a wide field of view (3614 $\times$ 2885 μm^2) to be able to acquire both the pillar-free region and complex medium at the same time. The sample is enclosed in a covering box with two red filtered windows for visualization. This prevents the microscope light from triggering phototaxis.

At the beginning microswimmers are homogeneously distributed in the chamber. A white LED light is switched on with a tunable orientation angle θ_ℓ with respect to the horizontal axis of the square lattice of pillars, as shown in Fig. 1. Due to negative phototaxis, microswimmers move away from the light source and go through the lattice of pillars as depicted in Fig. 1.
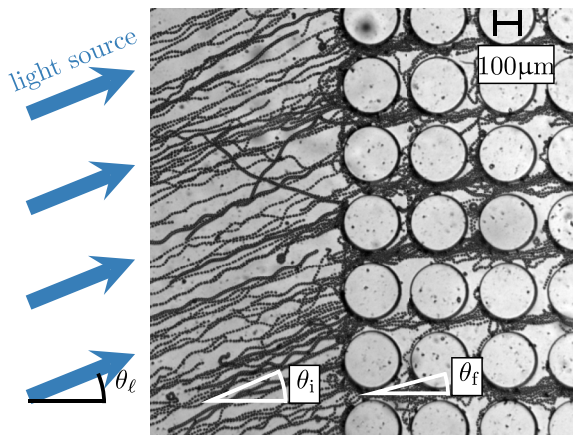
FIG. 1. Trajectories of phototactic microalgae CR through a microfluidic device. A LED light-beam source is used with a tunable incidence angle θ_ℓ with respect to the horizontal x axis of the square lattice of pillars. CR respond to the light stimulus through negative phototaxis and flee from the light source. In the pillar-free region, their swimming direction θ_i is on average directed along the light, i.e., $\bar{\theta}_i \sim \theta_\ell$. After entering the pillar lattice, successive reorientations of swimmers cause a distribution of swimmer trajectories with orientations θ_f and an average swim orientation $\bar{\theta}_f$.

III. EXPERIMENTAL RESULTS

Particle tracking is performed with the library Trackpy [31,32]. Orientations of microswimmers can then be extracted as the mean orientation of a trajectory over 0.5 s.

Figure 2 shows the distribution of the orientation of microswimmer trajectories in a pillar-free medium, as well as examples of swimmer trajectories in the inset. In the pillar-free region, the average swimming direction $\bar{\theta}_i$ corresponds to the orientation θ_ℓ of the light beam. The maximum of the orientational distribution around the direction of the light beam is found to be close to a
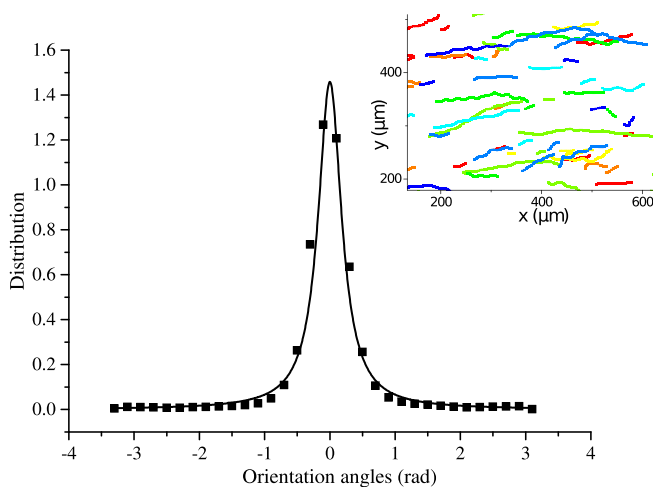

FIG. 2. The distribution of CR swimming directions in a pillar-free medium in the presence of a light source positioned at the left side with an incidence angle $\theta_\ell = 0$. The inset shows swimmer trajectories. The solid line is the distribution given by Eq. (1).

truncated Lorentzian distribution as previously shown in Ref. [33],

$$\Psi(\theta) = \frac{\Gamma}{2\pi} \frac{1}{\frac{\Gamma^2}{4} + \theta^2}, \tag{1}$$

where we obtain $\Gamma = 0.436\,\mathrm{rad} = 25°$ for the full width at half maximum.

As shown in Fig. 3 the distribution of the swimmer-orientation angles θ_f within the pillar lattice and therefore the mean swimming-direction $\bar{\theta}_\mathrm{f}$ depend on the angle θ_ℓ of the light beam. We show for four different values of $\theta_\ell \sim \bar{\theta}_\mathrm{i} = 10°, 27°, 56°, 87°$ in Fig. 3(a) examples of trajectories of the CR swimmer. In Fig. 3(b) we show for these four angles simultaneously the distribution of θ_f within the pillar lattice and θ_i in the pillar free range. The distributions of θ_f are found to be slightly narrower when the incident beam of light is oriented toward the lattice axes $\theta_\ell \approx 0°$ (or $\theta_\ell \approx 90°$). In these cases the trajectories through the pillar lattice follow the directions of corridors aligned with the light direction. For other values of θ_ℓ the angular distribution of θ_f is broader since CR are scattered by the pillar lattice. Therefore, we find in the pillar region $\bar{\theta}_\mathrm{f} \approx \theta_\ell$ when $\theta_\ell \approx 0°$ or $\theta_\ell \approx 90°$. On the contrary, for other angular values, the mean orientation $\bar{\theta}_\mathrm{f}$ deviates from $\bar{\theta}_\mathrm{i}$ since CR are scattered by the pillars away from the light direction. The maximum deviation occurs around $\theta_\ell \approx 30°$ where we find the deflection $\bar{\theta}_\mathrm{f} - \bar{\theta}_\mathrm{i} \approx 10°$, as can be seen in Fig. 4. Note that the curve is symmetric with respect to $\theta_\ell = 45°$, where we find $\bar{\theta}_\mathrm{f} \approx \theta_\ell$. By comparing our experimental results with numerical simulations we would like to understand on the one hand the role—if any—of HI and on the other hand the role of the intrinsic noise on the reorientations of the cells away from the light direction, i.e., the full width Γ of the distribution $\Psi(\theta)$ in Fig. 2.

IV. NUMERICAL SWIMMER MODEL

To further understand the observed deflection behavior shown in Fig. 4 we complement in this section our experimental results by a numerical analysis of a swimmer model of CR introduced in Sec. IV A and described in the Appendix. An analysis of the swimmer trajectories and their orientational distributions provides a basic picture of swimmer deflection and a thorough foundation of the analytical model given in Sec. V.

A. Swimmer model

For our numerical analysis we introduce a force dipole model for CR algae as illustrated in Fig. 5. The spherical body of radius a is impenetrable for the fluid and experiences a drag during its motion through the fluid. The flagella are located in a region of radius $\frac{4}{3}a$ with a distance $\frac{5}{3}a$ to the body-center. This region—unlike the body—is permeable for the fluid but is taken into account for hard core interactions with other swimmers or obstacles and mimics the excluded volume shape for the region covered by the flagella motion [34–37]. A doublet of forces is applied to the fluid both by flagella and the body (Fig. 5). The resulting flow-profile is shown in Fig. 12 in the Appendix and resembles the experimentally observed averaged flow profile of a CR algae [38] moving at a velocity V_0.

For the equations of motion described in Appendix A we use a 3D-Lattice Boltzmann (LB) solver [39] that covers the full hydrodynamics between swimmers and obstacles or walls. We also use a dissipative collision model to test the effect of pure collisional interactions between motile particles and the pillar wall without the influence of HI. In both cases, the phototaxis is modeled as a preferential direction of motion: each swimmer is, after an exponentially distributed time of mean τ_ph, reoriented toward a direction θ randomly drawn from a Lorentzian distribution of mean θ_ℓ (restricted to $-\pi < \theta < \pi$, with $\theta = 0$ corresponding to the x axis), that reproduces the truncated Lorentzian distribution shown in Fig. 2. The average time τ_ph is chosen as $\approx \frac{70a}{V_0}$, close to the experimental value (2s). α is then defined as the probability per unit of time of reorientation events $\alpha = 1/\tau_\mathrm{ph}$.
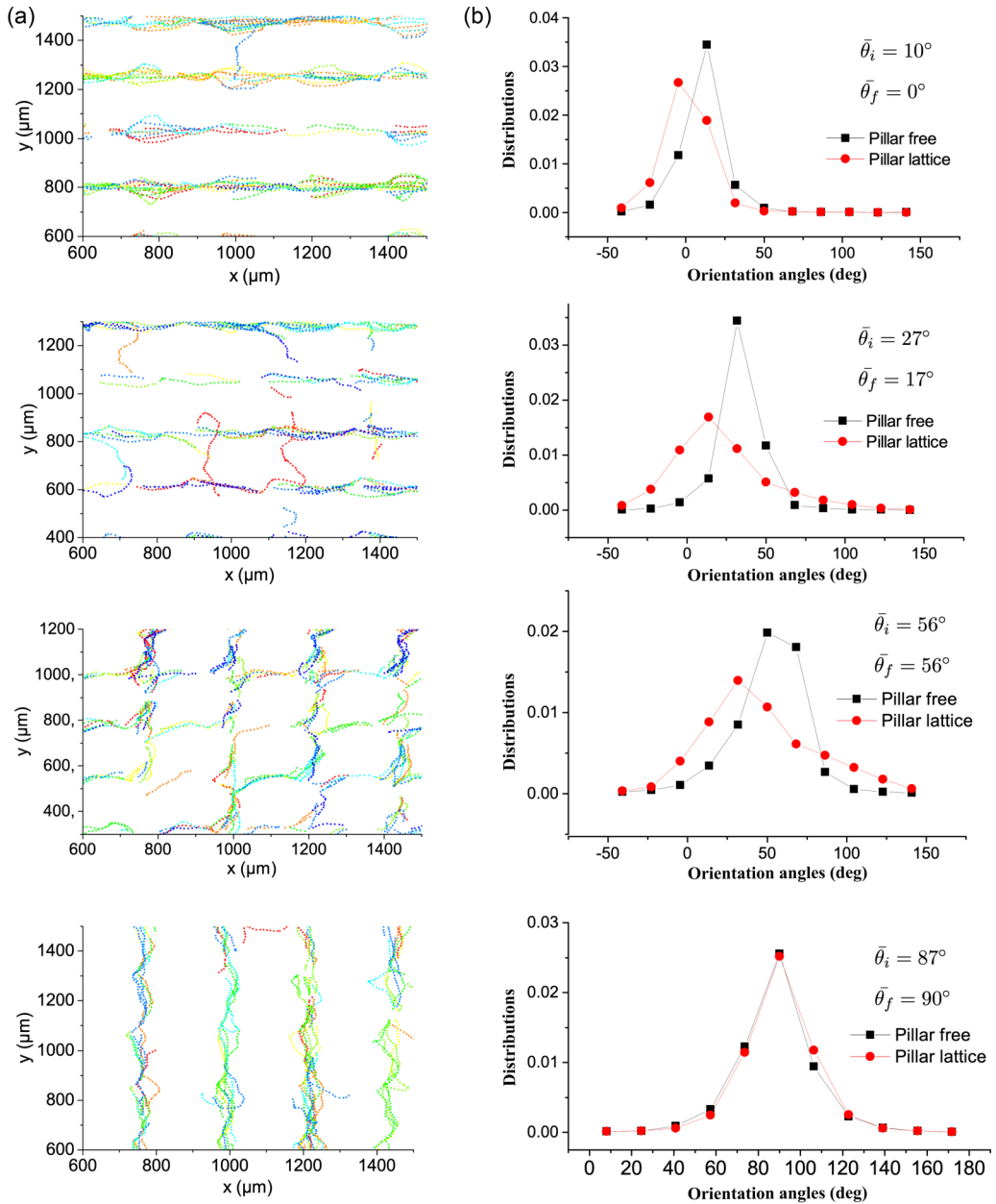
FIG. 3. The left column (part a) shows, for four examples of different incident angles $\theta_\ell \sim \bar{\theta}_I$, experimentally tracked trajectories of CR swimmers through the pillar lattice. For the same four angles, the right column (part b) shows the distributions of the CR-trajectory orientations through the pillar lattice, described by θ_f, and they are compared with the distribution of CR-trajectory orientation θ_i in the pillar free range.

The model swimmer is immersed in a simulation cuboid domain with in-plane periodic boundary conditions and with a single cylindrical pillar placed in the middle of the domain, which reproduces the exact proportions of the experiment.
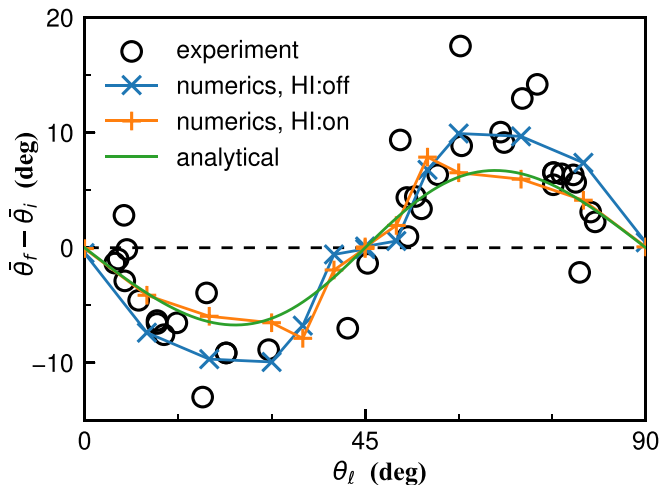
FIG. 4. The difference $\bar{\theta}_f - \bar{\theta}_i$ between the mean swimming direction $\bar{\theta}_f$ through the pillar lattice is shown as a function of the mean orientation $\bar{\theta}_i$ through the pillar free range. The experimental data are given by black circles. The numerical results from Sec. IV without hydrodynamic interactions (HI) are given by the blue symbols and with HI by the red symbols (for $\Gamma = 25°$). The green solid curve shows the result for the analytical model from Sec. V for $A_3 = 0.174$ from Eq. (8) with $D_R = 0.37 \text{ s}^{-1}$, $\alpha = 0.33 \text{ s}^{-1}$, and $\lambda_0 = 2.09 \text{ s}^{-1}$.

B. Numerical deflection of trajectories

For the numerical deflection data, we place a swimmer with random initial position and direction in the simulation region. We simulate the trajectories for different initial conditions for each value of θ_ℓ. From the averaged swimming direction, we extract the deflection angle $\bar{\theta}_f - \theta_\ell$. This is repeated for different light beam angles $0 < \theta_\ell < \pi/4$. For the data in the range of $\pi/4 < \theta_\ell < \pi/2$ we
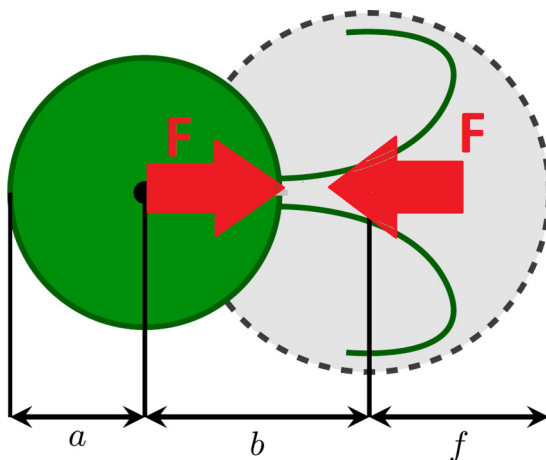
FIG. 5. Sketch of a model of the swimmer CR as used in simulations. The swimmer, described in more detail in Appendix A 1, consists of a hard impenetrable sphere of radius a (green). It is complemented by a sphere of radius $f = \frac{4}{3}a$ at a distance $\frac{5}{3}a$ from the body center, that covers the range of flagella motion: It is permeable for the fluid but hardcore repulsive for objects like other swimmers. A doublet of forces is exerted by the swimmer on the fluid.

FIG. 6. Sketch of the swimmer scattering by pillars. A swimmer starts at the position $\mathbf{r}_0$ with initial angle θ_0, corresponding to an initial direction $\mathbf{e}_i$. Here we have sketched 12 different directions $\mathbf{e}_i$ at the same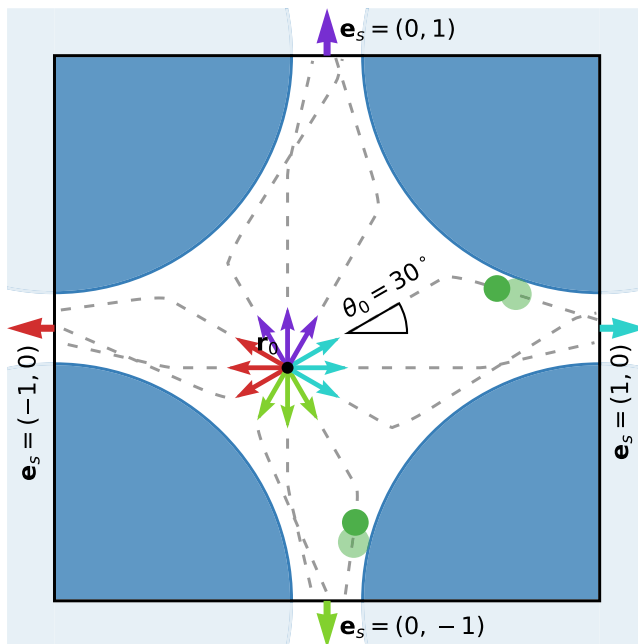 $\mathbf{r}_0$. The swimmer trajectories (gray dashed lines) are then determined via DCM and swimmers (sketched as green circles) may be deflected by the pillars. We track the trajectories until a swimmer leaves the unit cell at one of the exits. The exit directions are $\mathbf{e}_s(\mathbf{r}_0, \theta_0) = \{(\pm 1, 0), (0, \pm 1)\}$ (cyan, red, violet, green arrows). A statistics on the exit vectors is obtained by repeating the simulation for many different $\mathbf{r}_0$ and θ_0.

generated the data from simulations in the range $0 < \theta_\ell < \pi/4$ by using the point symmetry of the system.

The swimmer trajectories are simulated either with the LB method, which takes the hydrodynamic interactions between the swimmer and the pillar walls into account or by the dissipative collision model (DCM), also described in Appendix A. The dependence of the deflection angle, i.e., deviation $\bar{\theta}_f - \bar{\theta}_i$ from the light beam orientation $\theta_\ell \sim \bar{\theta}_i$ is shown in Fig. 4 together with the experimental data. Surprisingly, the results of both simulation approaches fit the characteristics of the experimental data quite well. Therefore, HI is not crucial on a qualitative level for the deflection process. It turns out that the occurrence of the deflection is mainly influenced by geometric properties and the statistical distribution of the reorientation. To get a better understanding of the underlying processes, we perform in the next section a statistical analysis of the scattering of a swimmer on a single pillar lattice without hydrodynamics and without a light beam. Later we extend the results on the scattering mechanism to full trajectories in the presence of light.

C. Deterministic scattering without light

To reach a basic understanding of the swimmer scattering leading to deflections as in Fig. 4 and to provide a foundation of the anisotropic analytical model in Sec. V, we analyze the deterministic trajectories of a model swimmer during a single scattering process (through a single pillar unit cell) in the absence of light. With this aim in mind, we place the model swimmer at different initial positions $\mathbf{r}_0$ and with different initial directions $\mathbf{e}_i$ within a unit of the pillar free space. The initial angle enclosed by $\mathbf{e}_i$ and the x axis is θ_0. We then determine the swimmer trajectory with the DCM. On their path the swimmers are scattered at the pillars due to the excluded volume effects. They leave a pillar unit cell through one of the four exits between the pillars, as shown in Fig. 6. This
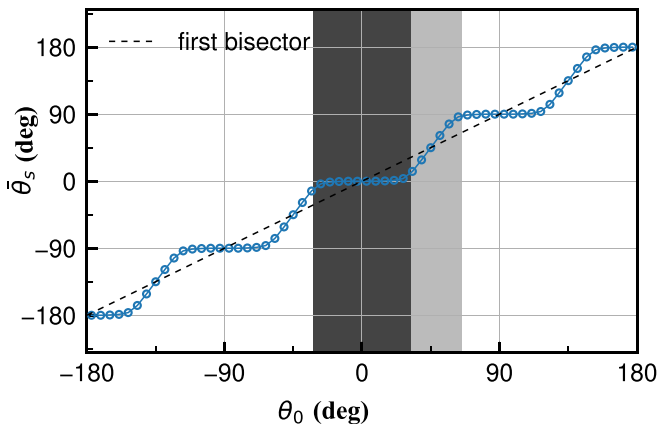
FIG. 7. Angle $\bar{\theta}_s$ after scattering in a single pillar cell, averaged over all initial positions $\mathbf{r}_0$ shown as a function of the initial swimmer orientation θ_0. For initial angles θ_0 around $0°$, $\pm 90°$, $180°$ the swimmers are deflected by pillars such that they are channeled along the symmetry axes of the pillar-lattice, which is the origin of the plateaus of $\bar{\theta}_s$. For initial angles $\theta_0 \sim \pm 45°$, $\pm 135°$ swimmers are equally likely deflected into neighboring exits, which results in $\bar{\theta}_s \sim \pm 45°$, $\pm 135°$.

procedure is repeated many times for different, uniformly distributed initial positions $\mathbf{r}_0$ and angles θ_0 to obtain the directions $\mathbf{e}_s(\mathbf{r}_0, \theta_0)$ at the exit as a function of the initial position and orientation. The four exit directions are $\mathbf{e}_s(\mathbf{r}_0, \theta_0) = \{(\pm 1, 0), (0, \pm 1)\}$, and the angle of the exit vector toward the positive x-axis is defined as θ_s ($\theta_s = \{0°, 180°, 90°, -90°\}$). Figure 7 shows the scattering (or exit) angle $\bar{\theta}_s$ averaged over the equally distributed initial positions $\mathbf{r}_0$ as a function of the initial orientation θ_0. Swimmers with $\mathbf{r}_0$ near the center between the four pillars and an initial orientation $\theta_0 \sim 0$ are very likely to leave the unit cell via the right exit $\mathbf{e}_s = (1, 0)$. With our simulations we find for initial angles in the range $0° < \theta_0 \lesssim 30°$ that swimmers are channeled by collisions with the pillars to the right exit $\mathbf{e}_s = (1, 0)$ as well. In this range of θ_0 the mean scattering angle $\bar{\theta}_s(\theta_0) \sim 0$ is nearly constant as indicated by the dark area in Fig. 7. The same holds for initial angles θ_0 around $\pm 90°$, $180°$ and plateaus are recovered. With an initial orientation $\theta_0 = 45°$ or $\pm 135°$ swimmers starting at different initial positions $\mathbf{r}_0$ are deflected in average equally likely either to the exit $\mathbf{e}_s = (1, 0)$ or to the exit $\mathbf{e}_s = (0, 1)$, which results in an average exit angle $\bar{\theta}_s \sim 45°$, cf. Fig. 7. With $\theta_0 \in [60°, 120°]$ we find $\bar{\theta}_s \sim 90°$.

Swimmers scattered by crossing a unit cell can be described by the following scattering function averaged over all initial positions in a unit cell: $\langle 1 - \mathbf{e}_i \cdot \mathbf{e}_s \rangle_{\mathbf{r}_0}$. The averaged function is shown in Fig. 8 as a function of the initial orientation θ_0. The scattering function almost vanishes with initial swimmer orientations close to one of the pillar-free axis and it has maxima along the 'diagonal' directions $\theta_0 \approx \pm 45°$, $\pm 135°$. The scattering function has a period of four in the range $[-\pi < \theta_0 < \pi]$, which reflects the symmetry axes of the pillar lattice. In addition, these numerical results for the scattering of a single swimmer provide a "microscopic" foundation for the assumption of a scattering rate $\lambda_0[1 - \cos(4\theta_0)]$ made in Eq. (3) of our phenomenological anisotropic scattering model, see Sec. V below. This form of the scattering rate reflects both the four-fold symmetry of the pillar lattice and the fact that swimmers are not scattered with their mean swim direction along pillar symmetry axes.

D. Deflection in the presence of light

The trajectory of CR can be described by a run-and-tumble walk with a preferred direction in the presence of light. That means a swimmer reorients after a certain time toward a new direction, loosing all information about the previous direction and path. Swimmers reorient on average every
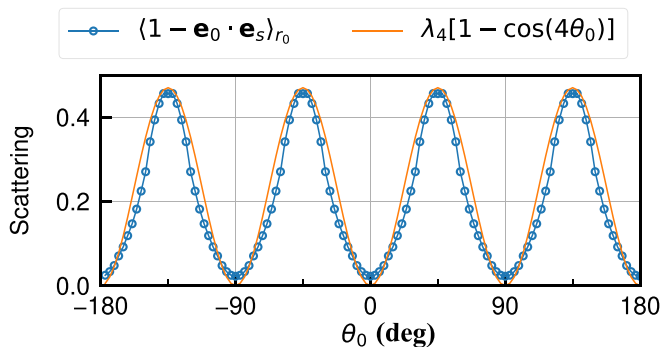
FIG. 8. The dots show the scattering function $\langle 1 - \mathbf{e}_i \cdot \mathbf{e}_s \rangle_{\mathbf{r}_0}$ from simulations of the scattering on a single pillar cell, averaged over the initial positions $\mathbf{r}_0$ as a function of initial direction $\mathbf{e}_i$ resp. the initial angle θ_0. Along the pillar free symmetry axes the scattering function vanishes and takes its maxima along the directions in between the symmetry axes. The full line is a fit by an expression that is proportional to $[1 - \cos(4\theta_0)]$.

$\sim 2\,$s toward the light orientation. With a speed of $100\ \mu$m/s and a length of the unit cell of $L = 200\ \mu$m, a swimmer reorients on average about once when crossing a pillar unit cell. Because it looses information about the past after this reorientation, the swimmer trajectories through several pillars can be described by repeated single scattering processes in a single pillar unit cell, provided one uses periodic boundary conditions. In the previous section we determined the function that gives the swimmers direction $\bar{\theta}_s(\theta_0)$ after a single scattering as a function of the initial direction θ_0. The initial direction of a scattering process is the direction after the tumbling. Since we know the probability distribution of swimmer reorientations given by Eq. (1), we can extract the mean swimming angle $\bar{\theta}_f$ of a swimmer's full trajectory by using the scattering function in a single unit cell. For this we need to weight the occurrence of the directions after scattering $\mathbf{e}_s(\theta_0)$ according to the tumbling probability distribution $\psi(\theta_0 - \theta_\ell)$ and get the mean swimming direction

$$\bar{\mathbf{e}}_f = \langle \bar{\mathbf{e}}_s(\theta_0)\psi(\theta_0 - \theta_\ell) \rangle_{\theta_0}, \tag{2}$$

with $\bar{\mathbf{e}}_s = \langle \mathbf{e}_s \rangle_{\mathbf{r}_0}$ and θ_f as the angle between $\bar{\mathbf{e}}_f$ and the x axes. Note that the norms of $\bar{\mathbf{e}}_s$ and $\bar{\mathbf{e}}_f$ are not necessarily equal to one. For very narrow distributions (i.e., small Γ) ψ is approximately a δ distribution. That means for the mean swimming direction $\bar{\mathbf{e}}_f \approx \langle \bar{\mathbf{e}}_s(\theta_0)\delta(\theta_0 - \theta_\ell) \rangle_{\theta_0} = \bar{\mathbf{e}}_s(\theta_\ell)$, so the angle $\bar{\theta}_f$ approaches the scattering function from the previous section. This case is shown in Fig. 9
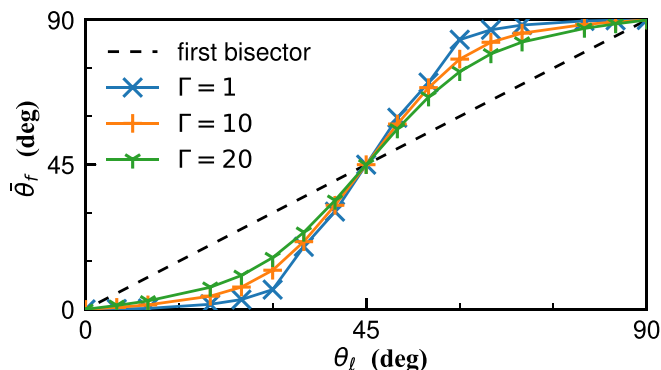

FIG. 9. The average deflection angle $\bar{\theta}_f$ extracted from the single scattering function is shown as a function of the light orientation θ_ℓ for three values of Γ corresponding to three different width of the Lorentz distribution, see Eq. (1).

(a) $\mathcal{P}_{DCM}$ (b) $\mathcal{P}_{LB}$
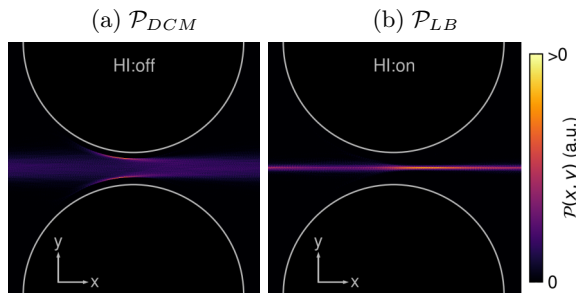

FIG. 10. Probability distribution $\mathcal{P}(x,y)$ of the position of a single swimmer in a unit cell for $\Gamma = 1°$, $\tau_{ph} \approx 8a/V_0$ and $\theta_\ell = 0$. (a) Without hydrodynamic interactions (DCM simulations), the interaction between swimmers and pillars is collision based, leading to a high probability to find particles at the contact positions near the pillars. (b) For simulations with HI (LB simulations), we find pronounced focusing between the pillars. This indicates that hydrodynamics helps the swimmers to avoid collisions with the obstacles.

(blue curve). For this small value of Γ, the mean swimming as a function of the light angle θ_ℓ has a rather steep behavior around $\theta_\ell \sim 45°$ and with a channeled regime $\bar{\theta}_f$ for $\theta_\ell \lesssim 30°$ similar to Fig. 8 in the range $0 < \theta_0 < 90°$. If we increase the distribution width Γ, then we see in Fig. 9 that the mean swimming direction $\bar{\theta}_f$ changes from the steplike, channeled function toward the first bisector. This behavior is caused by the distribution ψ. If Γ is small, then the initial directions $\mathbf{e}_s$ nearly always point toward the light direction. Therefore, if the light is along a symmetry axis, then the scattering of the swimmers is with a high probability such that they are channeled through the pillar lattice along a symmetry axis. If we choose a broad reorientation distribution width Γ, then even for a light orientation and the initial orientations $\mathbf{e}_i$ close to a symmetry axis it becomes with increasing Γ more and more probable that swimmers are scattered away from the respective symmetry axis. Thus, the mean swimming direction tends toward the first bisector for large Γ.

This is a crucial insight: the width of the Lorentz distribution determines the steepness of the shape of $\bar{\theta}_f(\theta_\ell)$. This is rather independent of whether the width of the distribution is just an intrinsic property of swimmers or possibly caused by other effects, such as hydrodynamic interactions between several swimmers as discussed in Sec. IV E. Furthermore we obtain a profound insight on the swimming statistics from the single-scattering function $\theta_s(\theta_0)$. This technique could probably be adapted to other problems, without necessity of simulating the swimmer trajectories but using information of absolute value of $\bar{\mathbf{e}}_s$, adapted weighting of the scattering function (e.g., position dependent), multiple folding for temporal correlation etc., to investigate the effect of depletion zones (e.g., caused by an imposed fluid flow), temporal correlation or different geometries of obstacle placement and many more.

E. Effect of the hydrodynamic interaction

To identify the influence of HI, we reduce the noise due to the tumbling in this section. This is achieved by simulations with a small distribution width of $\Gamma = 1°$ and a reduced tumbling time of $\tau_{ph} \approx 8a/V_0$.

The effects of HI becomes important for the interaction between swimmers and pillars. We show in Fig. 10 the probability distribution $\mathcal{P}(x,y)$ of the position of a guided single swimmer for $\theta_\ell = 0$. In Fig. 10(a) the probability distribution $\mathcal{P}(x,y)$ is shown for the case without HI between a swimmer and the pillars. This distribution is considerably broader than in Fig. 10(b) where in LB simulations the HI between pillars and swimmers is taken into account.

The effect of an enhanced swimmer channeling via HI is also confirmed by the deflection curves $\bar{\theta}_f(\theta_\ell)$ for single swimmers in Fig. 11. The simulation of a single swimmer with HI (green curve)
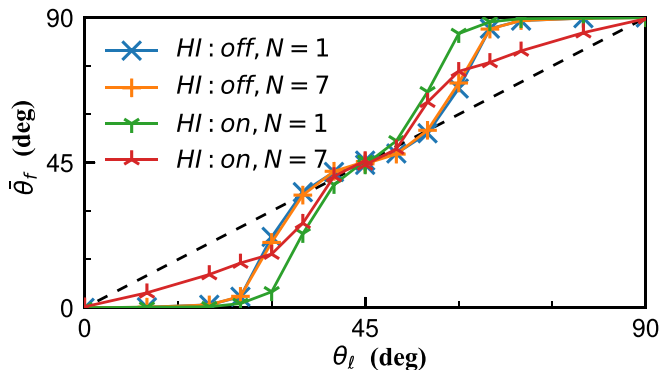
FIG. 11. Deflection curves for simulations with different numbers ($N = 1, 7$) of swimmers in a unit cell of the pillar lattice for $\Gamma = 1$ and $\tau_{\mathrm{ph}} \approx 8a/V_0$. For the simulations without HI, there is no difference for one or seven swimmers in a unit cell. In the case with HI in LB simulations the deflection curve is far less step for seven swimmers than for one swimmer (see text).

shows up to an angle $\bar{\theta}_\ell \sim 30°$ a channeling behavior while swimmers without HI (blue curve) escape channeling already at about $\bar{\theta}_{\mathrm{f}} \approx 20°$.

The influence of hydrodynamic interactions becomes also significant in the case with several swimmers in a unit cell. In Fig. 11 we compare the mean deflection $\bar{\theta}_{\mathrm{f}}$ obtained by simulations for a single swimmer without HI (blue curve), with the deflection of a single swimmer out of seven swimmers (orange) without HI. There is no significant difference.

When HI are taken into account the situation for a single swimmer and seven swimmers in a unit cell is rather different. As mentioned, the channeling of a swimmer is stronger in the case with than without HI. However, the deflection curve $\bar{\theta}_{\mathrm{f}}(\theta_\ell)$ of a single swimmer out of seven swimmers is in the case with HI less steep than for a single swimmer with HI. Moreover, it is also less steep than for swimmers without HI.

This can be explained as follows: The hydrodynamic interaction between different swimmers is of nonlinear nature. It is well known that nonlinear interactions between several particles cause a more complex dynamics than one obtains for a single particle. Hence, the HI between the swimmers act like an additional external noise source on a single swimmer. This additional noise does not depend on the orientation of the light nor on the intrinsic random reorientations swimmers. However, the hydrodynamic interactions between the swimmers cause additional reorientations of the single swimmer. The HI driven additional reorientations have a similar effect as a broader Lorentz distribution on a single swimmer. Therefore a broader reorientation Lorentz distribution has on a single swimmer a similar effect as the hydrodynamic interactions between swimmers having a narrower distribution. In both cases the deflection curve $\bar{\theta}_{\mathrm{f}}(\theta_\ell)$ is less steep as confirmed by the red curve in Fig. 11 and the green curve in Fig. 9. Therefore the strength of noise on the swimmer reorientations flattens the curve $\bar{\theta}_{\mathrm{f}}(\theta_\ell)$ independently of the nature of the reorientations.

V. ANALYTICAL MODELING

A. A swimmer model in an anisotropic scattering medium

We consider a simple theoretical model consisting of a self-propelled particle immersed in an effective anisotropic scattering medium [40]. The self-propelled particle is characterized by its 2D position **r** and an angle θ defining its direction of motion. The particle moves at a constant speed v_0. In the spirit of the numerical model studied in Sec. IV, we first neglect angular diffusion, and retain only the two main physical ingredients which are the scattering by the pillars and the random reorientations toward the direction of light. To make the problem tractable, the lattice of pillars

is modeled as an effective anisotropic scattering medium by following Ref. [40]. Guided by the numerical simulations of Sec. IV C (see Fig. 8), we choose a scattering rate

$$\lambda(\theta) = \lambda_0[1 - \cos(4\theta)], \tag{3}$$

that depends on the orientation θ of the self-propelled particle. Note that the scattering rate $\lambda(\theta)$ is not identical, but rather proportional to the scattering function defined in Sec. IV C. The proportionality factor is expected to be of the order of v_0 divided by the unit pillar cell size. After a scattering event, the new angle θ' is randomly chosen from a uniform distribution over the interval $(-\pi, \pi]$. The effective medium is homogeneous (though anisotropic), meaning that there are no explicit pillars, and scattering takes place with a probability rate $\lambda(\theta)$. It can thus occur at any place, and time intervals between stochastic scattering are exponentially distributed, with a mean value $1/\lambda(\theta)$. The form Eq. (3) of the scattering rate implies that particles can travel freely, without being scattered, when their direction of motion is aligned either with the x or y axis.

In addition, we assume that the particle tends to reorient stochastically during its motion to a direction, defined by an angle θ_ℓ with the x-axis, opposite to the direction of the light source. For convenience, we call it below the direction of the light source, even though the swimmer actually moves away from the light source. To be more specific, reorientation events occur with a probability $\alpha = 1/\tau_{\rm ph}$ per unit time, and the new orientation θ' is chosen here exactly as the direction θ_ℓ of the light source. Using periodic boundary conditions, we also assume that the system reaches a spatially homogeneous state. In this minimal model, the average direction of motion of the self-propelled particles can be computed exactly (see Appendix B), and it is found that the average angle $\bar{\theta}_{\rm f}$ within the scattering medium is equal to the angle θ_ℓ defining the direction of the light source. Hence, there is on average no deflection by the scattering medium. This means that the present minimal model is not able to reproduce, even qualitatively, the deflection phenomenon observed in the experiment and in the numerics. The physical ingredients that have been neglected here are notably the angular diffusion of the orientation of the self-propelled particle, and the angular fluctuations in the reorientation along the light direction. We will see below that taking into account these sources of noise is key to reproduce the phenomenology observed in the experiment and numerical simulations.

B. Swimmer model in an anisotropic scattering medium with random reorientations

We now slightly generalize the above model, by introducing angular diffusion in the motion of the swimmer, as well as some randomness in the angle chosen when reorienting in the light direction. We thus start by considering an active Brownian particle [41] such that in the absence of scattering medium, the angle θ has a purely diffusive dynamics

$$\dot{\mathbf{r}} = v_0 \mathbf{e}(\theta), \quad \dot{\theta} = \xi(t), \tag{4}$$

where $\xi(t)$ is a white noise satisfying $\langle \xi(t) \rangle = 0$ and

$$\langle \xi(t)\xi(t') \rangle = 2D_{\rm R}\,\delta(t - t'). \tag{5}$$

The angular diffusion coefficient is related to the persistence time τ by $\tau = 1/D_{\rm R}$. In the presence of scattering medium, the angle θ is subjected as in the previous model to a random scattering with a rate $\lambda(\theta) = \lambda_0 - \lambda_0 \cos(4\theta)$, the angle θ' after scattering being uniformly distributed. In addition, the reorientation process is also assumed to be noisy, in the sense that the angle θ' after reorientation is randomly chosen from a distribution $\psi(\theta' - \theta_\ell)$ centered around the direction θ_ℓ of the light source, similarly to the model used in Ref. [33] that reproduces the angular distribution of Fig. 2. For simplicity, we assume that the distribution ψ is symmetric, i.e., $\psi(-\theta) = \psi(\theta)$.

In this model, the deflection angle can no longer be computed exactly. However, it can be evaluated using an approximation scheme, valid in a regime where the angular diffusion is not too small (i.e., $9D_{\rm R} \gtrsim \lambda_0 + \alpha$). Under this approximation, we can evaluate the deflection angle ϕ

defined as

$$\bar{\theta}_{\mathrm{f}} = \theta_\ell + \phi \tag{6}$$

through the relation

$$\tan\phi = -\frac{\lambda_0 A_3 \psi_3 \sin(4\theta_\ell)}{2\psi_1 + \lambda_0 A_3 \psi_3 \cos(4\theta_\ell)} . \tag{7}$$

Here, the notation A_3 denotes

$$A_3 = \frac{1}{9D_{\mathrm{R}} + \lambda_0 + \alpha}, \tag{8}$$

and ψ_k is the Fourier coefficient of the distribution $\psi(\theta)$ in Fig. 2 obtained experimentally:

$$\psi_k = \int_{-\pi}^{\pi} d\theta \, \psi(\theta) \, \cos(k\theta). \tag{9}$$

The derivation of these results is reported in Appendix B. Consistently with the experimental results, the deviation ϕ vanishes when the angle θ_ℓ of the light source is a multiple of $\frac{\pi}{2}$. Before focusing on matching this theoretical model with the experimental results, let us briefly discuss the behavior of the deflection ϕ with the parameters of the model. We note that the angular diffusion as well as the width of the angular distribution $\psi(\theta)$ after reorientation, play a key role in determining the overall amplitude of the deflection. This result is consistent with the observation that the noise also plays an important role in determining the deflection in the numerical simulations reported in Sec. IV. As mentioned above, the approximate expression of ϕ in Eq. (7) has been derived under the assumption $9D_{\mathrm{R}} \gtrsim \lambda_0 + \alpha$. Under this hypothesis, we see that the deflection ϕ decreases when increasing the angular diffusion coefficient D_{R}. Similarly, increasing the width of the distribution $\psi(\theta)$ of the swimming angle θ after reorientation leads to a decrease of the deflection ϕ, in qualitative agreement with the results of numerical simulations displayed on Fig. 9. Hence we again observe that increasing the noise in the dynamics reduces the amplitude of the deflection (although, as noted above, at zero angular noise the deflection also vanishes). In other words, a finite amount of noise in the angular dynamics is needed to observe a deflection. This deflection disappears both for small (see Sec. V A) and large noise. This can be understood intuitively as follows. Angular diffusion actually allows the particle to explore orientations that are close to the direction θ_ℓ of light. Through this local angular exploration, the particle can "feel" the anisotropy of the scattering rate $\lambda(\theta)$. If the particle has an angle θ slightly larger than θ_ℓ ($0 < \theta_\ell < \pi/4$), then it may for instance be scattered more than if it has an angle θ slightly smaller than θ_ℓ. In this case, this results in a slight deflection toward angles smaller than θ_ℓ.

We now turn to a comparison of the model with the experiment. We provide in Fig. 4 the mean deflected angle $\bar{\theta}_{\mathrm{f}}$ as a function of θ_ℓ and compare it to our experimental results, where θ_ℓ is evaluated as the mean incidence angle $\bar{\theta}_{\mathrm{i}}$. We fixed the parameters of the analytical fit of the experimental data using previously determined parameters: we fixed $\lambda_0 = 2.09\,\mathrm{s}^{-1}$ associated with a medium where $d = 30\,\mu\mathrm{m}$, the rotational diffusion coefficient $D_{\mathrm{R}} = 0.37\,\mathrm{s}^{-1}$ (both referenced in Ref. [40]), and the tumbling rate toward the light beam $\alpha = 0.33\,\mathrm{s}^{-1}$ [33]. The distribution of orientations in Fig. 2 is shown to be well described by a truncated Lorentzian, providing a full width at half maximum of $\Gamma = 0.436\,\mathrm{rad} = 25°$. Then Eq. (9) yields the values $\psi_1 = 0.809$ and $\psi_3 = 0.521$ for the Fourier coefficients of the distributions $\psi(\theta)$. We obtain a quite good quantitative agreement with the experiments and the numerical simulations, demonstrating that we can explain this deflected phototactic swimming by means of a simple stochastic model.

Note that in the numerical model studied in Sec. IV, no angular diffusion has been explicitly introduced. However, one may interpret the angular diffusion as an effective one emerging from the collisions with the pillars. In the analytical model, collisions with the pillar are modeled with a scattering rule where the angle after collision is randomly chosen in an isotropic way. Yet, in the numerical simulations, the angle after collision with a pillar is correlated with the angle before

collision. A minimal way to account for this correlation is to introduce an effective angular diffusion that comes on top of the scattering rate.

VI. DISCUSSION AND CONCLUSION

We investigated in the presence of a light stimulus the mean swimming direction of a phototactic microalga *Chlamydomonas reinhardtii*, described by the angle $\bar{\theta}_\mathrm{f}$, through a square lattice of pillars with two symmetry axes along the x and y axes. We designed the experimental set up so that the distance between pillar centers is comparable to the persistence length of the swimmers, to allow for an interplay between the natural angular diffusion of swimmer motion and the scattering by the pillars. We used in experiments a CR species that swims away from a light source. Their swimming direction is on the one hand guided by the direction of light, described by θ_ℓ, and on the other hand by the pillar symmetry axes. We found an interesting nonlinear θ_ℓ-dependence of the difference $\bar{\theta}_\mathrm{f} - \theta_\ell$. It vanishes for the light beam parallel to one of the symmetry axes (including the diagonal one) and this angle difference shows maxima with the light beam making an angle $\theta_\ell \sim 30°$ with the x axis.

To further understand the origin of the nonlinear θ_ℓ-dependence of $\bar{\theta}_\mathrm{f}$-θ_ℓ, we complemented our experiments by simulations of a swimmer model and by an analytical modeling that contains the key ingredients leading to swimmer deflection in a square pillar lattice.

In our simulations we either neglected or took into account the HI between pillars and swimmers. We found for single swimmers (diluted limit), that there is no qualitative difference with and without HI. In simulations it is also possible to vary systematically the random reorientation distribution of swimmers, which is an intrinsic property of CR. We found that this reorientation distribution has a strong impact on the θ_ℓ-dependence of $\bar{\theta}_\mathrm{f}$-θ_ℓ. For a narrow reorientation distribution we found a strong channeling effect, i.e., with deviations of θ_ℓ up to about $30°$ from the x or the y axes the swimmers moved essentially along the x or the y axes. This channeling effect is reduced by choosing wider swimmer reorientation distributions. Thus, a narrow reorientation distribution of swimmers, which is associated with a strong channeling effect, is the origin of a strong nonlinear θ_ℓ-dependence of the difference $\bar{\theta}_\mathrm{f}$-θ_ℓ.

The reorientation distribution of single swimmers is specific to the chosen species. However, as we have shown by numerical simulations, it also depends on the hydrodynamic interaction between several swimmers. If there are several swimmers in a pillar unit cell, they mutually influence via the nonlinear hydrodynamic interactions their individual dynamics and these HI act like a broadening of their specific reorientation distribution. This broadening effect leads to a less pronounced nonlinear θ_ℓ dependence of the deflection $\bar{\theta}_\mathrm{f}$-θ_ℓ. Therefore, the width of the reorientation distribution is a central parameter that needs to be included in the models.

We also performed a numerical scattering statistics of a single model swimmer in the pillar lattice. The resulting scattering function in Fig. 7 is fitted by a phenomenological scattering rate given by Eq. (3), that was introduced earlier with an analytical model of swimmer scattering in an anisotropic medium [40], also described in Sec. V A. Hence, with our numerical scattering statistics for single swimmers in the pillar lattice we found a "microscopic" foundation for the phenomenological scattering rate used in the analytical model.

Along this reasoning we identified the two essential parameters for the deflection of light guided swimmers through a square pillar lattice. This is one phenomenological scattering rate and a parameter for the width of the random reorientation of swimmers, independent of its origin, which can be purely intrinsic or a combination of intrinsic noise with HI effects. This basic understanding of the swimmer deflection in a pillar lattice is condensed in our analytical model. Taking the two parameters of the basic model as fit parameters we obtain a very good agreement with the experimental results. A great advantage of our analytical model is its simple handling and is also appropriate for different pillar sizes and distances through an associated effective scattering medium. It can also be adapted to different geometries (triangular, hexagonal, etc.) by taking into account the appropriate angular dependence of $\lambda(\theta)$.
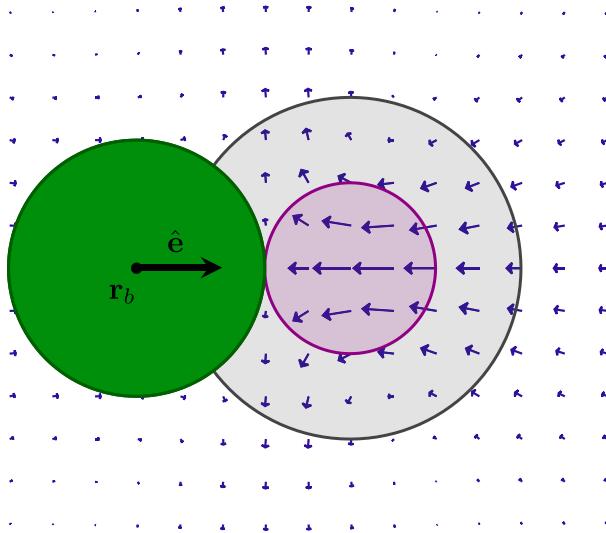
FIG. 12. Numerical representation of a CR at position $\mathbf{r}$ and swimming direction $\hat{\mathbf{e}}$. The driving force $\mathbf{f}_d$ acting on the swimmer body is balanced by applying a negative force $-\mathbf{f}_d$ at the center of the flagella moving range onto the fluid (purple circle). The blue arrows show the resulting flow-field for simulations with the LB method, which resembles the time-averaged field of a Chlamydomonas [38].

The identified dependence of the swimmer deflection on the reorientation distribution of swimmers in a pillar lattice may be also used for separating swimmers with a different reorientation distribution by guiding them via a light source through a pillar lattice.

ACKNOWLEDGMENT

APPENDIX A: NUMERICAL METHOD

1. Swimmer model

The swimmer is modeled as a force-dipole swimmer (Fig. 12) with the orientation $\hat{\mathbf{e}}$. For the force calculation, we consider excluded volume forces $\mathbf{f}_e(\mathbf{r})$ for both, the flagella and the body. Here, $\mathbf{f}_e(\mathbf{r})$ is the short-range repulsive part of the Weeks-Chandler-Anderson potential [42] for a separation distance $\mathbf{r}$. The driving force $\mathbf{f}_d = f_d \hat{\mathbf{e}}$ acting on the body is balanced by applying a negative force $-\mathbf{f}_d$ on the fluid at the position of the flagella (see Fig. 12). We assume that the flagella have negligible mass and the center of mass is located at the center of the body, resulting in a torque due to the excluded volume force with center at $\mathbf{r}_f$. The total, nonhydrodynamic forces $\mathbf{f}_b$ and torques $\mathbf{t}_b$ acting on the swimmer body are given by

$$\mathbf{f}_b = \mathbf{f}_d + \sum_i [\mathbf{f}_e(\mathbf{e}_i - \mathbf{r}_b) + \mathbf{f}_e(\mathbf{e}_i - \mathbf{r}_f)], \tag{A1}$$

$$\mathbf{t}_b = \sum_i (\mathbf{r}_f - \mathbf{r}_b) \times \mathbf{f}_e(\mathbf{e}_i - \mathbf{r}_f), \tag{A2}$$

where we sum over all other objects i at positions $\mathbf{e}_i$ to be considered for excluded volume interactions (i.e., other swimmers and obstacles).

2. Equations of motion

As fluid solver we use two different models, the dissipative collision model (DCM) and the Lattice-Boltzmann (LB) method. Both require as input the positions, forces and torques $\mathbf{r}_b, \mathbf{f}_b, \mathbf{t}_b$ of the body and the positions $\mathbf{r}_f$ and forces $\mathbf{f}_f = -\mathbf{f}_d$ at the flagella position at time t. As output, they provide the velocities $\mathbf{v}_b$ and angular velocities $\mathbf{w}_b$ for the new time $t + \Delta t$. The new positions and swimming-directions are then updated via an Euler's integration:

$$\mathbf{r}_b(t + \Delta t) = \mathbf{r}_b(t) + \Delta t\, \mathbf{v}_b(t), \tag{A3}$$

$$\hat{\mathbf{e}}(t + \Delta t) = \mathbf{R}(\mathbf{w}_b(t)\, \Delta t)\, \hat{\mathbf{e}}, \tag{A4}$$

where $\mathbf{R}(\boldsymbol{\alpha})$ is the rotation defined by the vector $\boldsymbol{\alpha}$.

a. Dissipative collision model (DCM): For the dissipative collision model, we only consider the driving force and collisions through excluded volume interactions while neglecting HI. We use the Stokes-drag of the particles to calculate the new angular and translational velocities as

$$\mathbf{v}_b(t + \Delta t) = \frac{\mathbf{f}_b}{6\pi \eta a}, \tag{A5}$$

$$\mathbf{w}_b(t + \Delta t) = \frac{\mathbf{t}_b}{8\pi \eta a^3}. \tag{A6}$$

For the simulations, we use as parameters $\eta = 1/6$ and a radius of $a = 3$.

b. Lattice Boltzmann (LB) method: For the simulations including HI, we utilize the LB method with the Bhatnagar-Gross-Krook (BGK) collision step which reproduces the full Navier-Stokes equation in the incompressible limit [43]. We calculate the phase-density $f_i(\mathbf{x}, t)$ of the fluid elements on a three-dimensional grid of positions $\mathbf{x} = (x, y, z)$ along the discrete directions $\mathbf{c}_i (i = 0, \ldots, 18)$ (D3Q19 model) with a spatial discretization of $\Delta x = 1$ and $\Delta t = 1$ for the temporal discretization. The evolution equation is given by [43,44]

$$f_i(\mathbf{x} + \mathbf{c}_i\, \Delta t, t + \Delta t) = f_i(\mathbf{x}, t) + \mathcal{C}, \tag{A7}$$

where

$$\mathcal{C} = \frac{1}{\tau}\big[f_i(\mathbf{x}, t) - f_i^{\mathrm{eq}}(\mathbf{x}, t)\big] \tag{A8}$$

is the BGK collision operator with the equilibrium distribution

$$f_i^{\mathrm{eq}}(\mathbf{x}, t) = \rho w_i\left[1 + \frac{\mathbf{c}_i \cdot \mathbf{u}}{c_s^2} + \frac{(\mathbf{c}_i \cdot \mathbf{u})^2}{2c_s^4} - \frac{\mathbf{u}^2}{2c_s^2}\right]. \tag{A9}$$

The time constant τ is linked to the fluid viscosity via $\nu = c_s^2 \Delta t(\tau - 1/2)$. The weighting factors w_i and the parameter c_s are constants with specific values for the chosen simulation model [43]. Walls are implemented with the standard bounce-back (bbk) scheme [45], which alters the evolution Eq. (A7), such as

$$f_{i'}(\mathbf{x}, t + \Delta t) = f_i(\mathbf{x}, t) + \mathcal{C} + \mathcal{W}, \tag{A10}$$

if f_i points into a wall, where i' is the antiparallel direction to i and $\mathcal{W} = 2w_i\rho \frac{\mathbf{c}_i \cdot \mathbf{u}_w}{c_s^2}$ accounts for the momentum exchange of a moving wall with velocity $\mathbf{u}_w$.

External volume forces linked to the out-of-lattice position of the swimmers are coupled to the fluid grid via the immersed boundary method using the four-point stencil [46], which provides the volume-forces $\mathbf{F}_v(\mathbf{x})$ at the fluid grid positions. For nodes with $\mathbf{F}_v \neq 0$, the collision operator

[Eq. (A7)] is extended by adding the Guo force-coupling term [47]

$$\mathcal{F} = \Delta t \left(1 - \frac{1}{2\tau}\right) w_i \left[\frac{\mathbf{c}_i - \mathbf{u}}{c_s^2} + \frac{(\mathbf{c}_i \cdot \mathbf{u})}{c_s^4}\mathbf{c}_i\right] \cdot \mathbf{F}_v. \tag{A11}$$

The fluid-density ρ and fluid-velocity $\mathbf{u}$ are obtained by

$$\rho = \sum_i f_i, \tag{A12}$$

$$\rho\mathbf{u} = \sum c_i \mathbf{f}_i + \frac{\Delta t}{2}\mathbf{F}_v. \tag{A13}$$

The swimmers body is implemented by setting links crossing the particle surface as moving-wall [48,49]. The wall velocity for those links is set to $\mathbf{u}_w(\mathbf{x}) = \mathbf{v}_b + \mathbf{w} \times (\mathbf{x} + \frac{1}{2}\mathbf{c}_i - \mathbf{r}_b)$. The hydrodynamic force $\mathbf{f}_h$ and torque $\mathbf{t}_h$ exerted from the fluid on the particle can then be calculated by summing all contributions of the momentum exchange between the fluid and wall-links over the surface of the body and eventual covered/uncovered forces (see Ref. [49] for more details). The new swimmer velocity is then given by Newton's law according to

$$\mathbf{v}_b(t + \Delta t) = \mathbf{v}_b(t) + \frac{\Delta t}{M}[\bar{\mathbf{f}}_h + \bar{\mathbf{f}}_b], \tag{A14}$$

$$\mathbf{w}_b(t + \Delta t) = \mathbf{w}_b(t) + \frac{\Delta t}{I}[\bar{\mathbf{t}}_h + \bar{\mathbf{t}}_b], \tag{A15}$$

where M is the mass of the swimmer body and I its moment of inertia while $\bar{\mathbf{f}}_h$ and $\bar{\mathbf{t}}_h$ are the forces and torques averaged over two intermediate time-steps as described in Ref. [49].

For the swimmer, we use the radius $a = 3$, the density $\rho = 1$ and a relaxation parameter $\tau = 1$. For the dipole-force, we choose $f_d = 0.25$ by using the technique described in Ref. [50] to find a reasonable swimming velocity which ensures low Reynolds dynamics while keeping simulation time short. This parameter results in a Reynolds-number of 0.39 and an error of less than two percent in a distance of one radius away from the Chlamydomonas.

APPENDIX B: ANALYTICAL MODEL

We provide in this Appendix a detailed analysis of the effective medium model defined in Sec. V of the main text, to evaluate analytically the deflection angle.

Assuming for simplicity spatial homogeneity, the dynamical distribution $P(\theta)$ of the swimmer angle θ satisfies the evolution equation

$$\partial_t P(\theta) = D_R \partial_\theta^2 P(\theta) - (\lambda(\theta) + \alpha)P(\theta) + \frac{1}{2\pi}\int_{-\pi}^{\pi} d\theta' \, \lambda(\theta')P(\theta') + \alpha\rho\psi(\theta - \theta_\ell). \tag{B1}$$

Equation (B1) takes into account three dynamical mechanisms: angular diffusion with diffusion coefficient D_R, anisotropic tumbling mechanism with rate $\lambda(\theta)$ (modeling the lattice of pillars as an effective scattering medium), and the reorientation against the direction of light with rate α and distribution $\psi(\theta - \theta_\ell)$ of the angle θ after reorientation. Angular diffusion contributes as a single term (the second derivative with respect to θ) in Eq. (B1). The anisotropic tumbling and reorientation against light mechanisms are jump processes, and thus each of them contributes with two terms, a positive gain term and a negative loss term, to the evolution equation.

We assume in the following that $P(\theta)$ is normalized as $\int_{-\pi}^{\pi} d\theta \, P(\theta) = \rho$, where ρ is the uniform density of swimmers. It is convenient to define the angular Fourier mode f_k of the distribution $P(\theta)$, as

$$f_k = \int_{-\pi}^{\pi} d\theta \, P(\theta) \, e^{ik\theta}. \tag{B2}$$

Note that $f_{-k} = f_k^*$, where the star indicates the complex conjugate. Expanding Eq. (B1) in Fourier modes, one gets for $k \neq 0$ (the equation for $k = 0$ is trivially valid in a spatially homogeneous state),

$$\partial_t f_k = -(D_R k^2 + \lambda_0 + \alpha) f_k + \alpha \rho \psi_k e^{ik\theta_\ell} + \frac{\lambda_0}{2} (f_{k+4} + f_{k-4}), \tag{B3}$$

where ψ_k is the Fourier coefficient of the distribution $\psi(\theta)$ of the angle θ after random reorientation to the light source [see Eq. (9) of the main text], and θ_ℓ is the average direction toward which the particle reorients. We wish to determine the average velocity $\mathbf{v}$ of particles in the presence of the light source. The velocity $\mathbf{v}$ is related to the Fourier mode f_1 through

$$\mathbf{v} = \frac{v_0}{\rho} (\text{Re} f_1, \text{Im} f_1). \tag{B4}$$

The average angle of motion of the microswimmers in the effective medium, corresponding to the direction of the velocity $\mathbf{v}$ is thus given by

$$\bar{\theta}_f = \text{Arg}(f_1), \tag{B5}$$

where the function $\text{Arg}(z)$ is the argument of the complex number z. We thus need to determine f_1 in the stationary homogeneous state. Dropping the time derivative term in Eq. (B3), one has to solve the infinite hierarchy of equations

$$f_k = A_k \left[\alpha \rho \psi_k e^{ik\theta_\ell} + \frac{\lambda_0}{2} (f_{k+4} + f_{k-4}) \right], \tag{B6}$$

where the parameter A_k is defined as

$$A_k = \frac{1}{k^2 D_R + \lambda_0 + \alpha}. \tag{B7}$$

In general, the hierarchy of Eqs. (B6) cannot be solved exactly, at least not in a simple way. However, in the specific case $D_R = 0$ (absence of angular diffusion) and $\psi_k = 1$ for all k, corresponding to a Dirac distribution $\psi(\theta)$, an exact solution can be found because Eq. (B6) becomes in this limit a simple recursion relation for the Fourier modes f_{4n+1} (other modes do not need to be considered). Solving this recursion relation to determine f_{4n+1} for all n, one eventually finds for f_1,

$$f_1 = \frac{\rho \alpha e^{i\theta_\ell}}{\lambda_0 + \alpha - \lambda_0 \cos(4\bar{\theta}_i)}, \tag{B8}$$

which implies $\bar{\theta}_f = \theta_\ell$. Hence in the absence of angular noise and with an infinitely sharp distribution $\psi(\theta)$, there is no deflection in the effective medium model.

In other cases, a simple solution cannot be found, and one has to resort to an approximation scheme. We discuss below a simple approximation scheme, together with its range of validity. We first note that if D_R is not too small as compared to $\lambda_0 + \alpha$, the coefficient A_k decays relatively rapidly when k is increased. A simple approximation scheme is thus to approximate A_k by zero beyond some order k. Using the previously reported values of D_R, λ_0 and α [33,40] (see also Sec. V), we find that for $k > 4$ the term $k^2 D_R$ starts to be dominant over $\lambda_0 + \alpha$, thus making A_k decay faster for higher values of k. We thus make the crude approximation $A_k \approx 0$ for $k > 4$. From Eq. (B6), this implies that one can neglect Fourier modes f_k with $|k| > 4$, leading to the following equations for f_1 and f_3,

$$f_1 = A_1 \left[\alpha \rho \psi_1 e^{i\theta_\ell} + \frac{\lambda_0}{2} f_3^* \right], \tag{B9}$$

$$f_3 = A_3 \left[\alpha \rho \psi_3 e^{3i\theta_\ell} + \frac{\lambda_0}{2} f_1^* \right]. \tag{B10}$$

Combining Eqs. (B9) and (B10), one obtains

$$f_1 = \frac{\alpha A_1 \rho}{1 - \frac{\lambda_0^2}{4} A_1 A_3} \left[\psi_1 + \frac{\lambda_0}{2} A_3 \psi_3 e^{-4i\theta_\ell} \right] e^{i\theta_\ell} . \tag{B11}$$

The prefactor in front of the bracket is always positive, and taking the argument of Eq. (B11) to evaluate $\bar{\theta}_f$ according to Eq. (B5), one finds

$$\bar{\theta}_f = \theta_\ell + \phi, \tag{B12}$$

where the deflection angle ϕ is determined by

$$\tan \phi = -\frac{\lambda_0 A_3 \psi_3 \sin(4\theta_\ell)}{2\psi_1 + \lambda_0 A_3 \psi_3 \cos(4\theta_\ell)} . \tag{B13}$$

Note that the deflection $\phi = 0$ when θ_ℓ is a multiple of $\frac{\pi}{2}$. According to the approximations made, the expression Eq. (B13) of the deflection angle is expected to be approximately valid for not too small angular diffusion coefficient D_R, that is, as long as $9D_R \gtrsim \lambda_0 + \alpha$, which is the case with the experimental values. For smaller D_R, the simple truncation procedure used above is no longer valid, and a larger number of Fourier modes should be retained in the approximation. Finding in an analytical way the approximate solution of the hierarchy of Eqs. (B6) is thus more difficult, and one would then need to resort to a numerical procedure to solve Eq. (B6). The above results are summarized in Sec. V of the main text.

---

[1] Y. H. An and R. J. Friedman, Concise review of mechanisms of bacterial adhesion to biomaterial surfaces, J. Biomed. Mater. Res. 43, 338 (1998).

[2] J. W. Costerton, P. S. Stewart, and E. P. Greenberg, Bacterial biofilms: A common cause of persistent infections, Science 284, 1318 (1999).

[3] S. Lecuyer, R. Stocker, and R. Rusconi, Focus on the physics of biofilms, New J. Phys. 17, 030401 (2015).

[4] H. P. Chu and X.-Y. Li, Membrane fouling in a membrane bioreactor (mbr): Sludge cake formation and fouling characteristics, Biotechnol. Bioeng. 90, 323 (2005).

[5] A. Marty, C. Roques, C. Causserand, and P. Bacchin, Formation of bacterial streamers during filtration in microfluidic systems, Biofouling 28, 551 (2012).

[6] R. Rusconi, S. Lecuyer, N. Autrusson, L. Guglielmini, and H. A. Stone, Secondary flow as a mechanism for the formation of biofilm streamers, Biophys. J. 100, 1392 (2011).

[7] A. Creppy, E. Clément, C. Douarche, M. V. D'Angelo, and H. Auradou, Effect of motility on the transport of bacteria populations through a porous medium, Phys. Rev. Fluids 4, 013102 (2019).

[8] G. Volpe, I. Buttinoni, D. Vogt, H.-J. Kümmerer, and C. Bechinger, Microswimmers in patterned environments, Soft Matter 7, 8810 (2011).

[9] O. Chepizhko and T. Franosch, Ideal circle microswimmers in crowded media, Soft Matter 15, 452 (2019).

[10] C. Jin, J. Vachier, S. Bandyopadhyay, T. Macharashvili, and C. C. Maass, Fine balance of chemotactic and hydrodynamic torques: When microswimmers orbit a pillar just once, Phys. Rev. E 100, 040601(R) (2019).

[11] D. Nishiguchi, I. S. Aranson, A. Snezhko, and A. Sokolov, Engineering bacterial vortex lattice via direct laser lithography, Nat. Commun. 9, 1 (2018).

[12] L. R. Huang, E. C. Cox, R. H. Austin, and J. C. Sturm, Continuous particle separation through deterministic lateral displacement, Science 304, 987 (2004).

[13] J. Bammert and W. Zimmermann, Dumbbell transport and deflection in a spatially periodic potential, Eur. Phys. J. E 28, 331 (2009).

[14] J. McGarth, M. Jimenez, and H. Bridle, Deterministic lateral displacement for particle separation: A review, Lab Chip 14, 4139 (2014).

[15] X. Garcia, S. Rafaï, and P. Peyla, Light Control of the Flow of Phototactic Microswimmer Suspensions, Phys. Rev. Lett. **110**, 138106 (2013).

[16] S. Rafai, L. Jibuti, and P. Peyla, Effective Viscosity of Microswimmer Suspensions, Phys. Rev. Lett. **104**, 098102 (2010).

[17] L. Jibuti, L. Qi, C. Misbah, W. Zimmermann, S. Rafai, and P. Peyla, Self-focusing and jet instability of a microswimmer suspension, Phys. Rev. E **90**, 063019 (2014).

[18] E. Lauga and F. Nadal, Clustering instability of focused swimmers, Europhys. Lett. **116**, 64004 (2017).

[19] O. Chepizhko and F. Peruani, Diffusion, Subdiffusion, and Trapping of Active Particles in Heterogeneous Media, Phys. Rev. Lett. **111**, 160604 (2013).

[20] C. Bechinger, R. Di Leonardo, H. Löwen, C. Reichhardt, G. Volpe, and G. Volpe, Active particles in complex and crowded environments, Rev. Mod. Phys. **88**, 045006 (2016).

[21] A. Chamolly, T. Ishikawa, and E. Lauga, Active particles in periodic lattices, New J. Phys. **19**, 115001 (2017).

[22] T. Bertrand, Y. Zhao, O. Bénichou, J. Tailleur, and R. Voituriez, Optimized Diffusion of Run-And-Tumble Particles in Crowded Environments, Phys. Rev. Lett. **120**, 198103 (2018).

[23] A. Morin, D. L. Cardozo, V. Chikkadi, and D. Bartolo, Diffusion, subdiffusion, and localization of active colloids in random post lattices, Phys. Rev. E **96**, 042611 (2017).

[24] M. Zeitz, K. Wolff, and H. Stark, Active brownian particles moving in a random lorentz gas, Euro. Phys. J. E **40**, 23 (2017).

[25] R. Alonso-Matilla, B. Chakrabarti, and D. Saintillan, Transport and dispersion of active particles in periodic porous media, Phys. Rev. Fluids **4**, 043101 (2019).

[26] E. H. Harris, *The Chlamydomonas Sourcebook: Introduction to Chlamydomonas and Its Laboratory Use* (Academic Press, San Diego, CA, 2009), Vol. 1.

[27] L. Jibuti, W. Zimmermann, S. Rafaï, and P. Peyla, Effective viscosity of a suspension of flagellar-beating microswimmers: Three-dimensional modelling, Phys. Rev. E **96**, 052610 (2017).

[28] M. Polin, I. Tuval, K. Drescher, J. P. Gollub, and R. E. Goldstein, Chlamydomonas swims with two "gears" in a eukaryotic version of run-and-tumble locomotion, Science **325**, 487 (2009).

[29] M. Garcia, S. Berti, P. Peyla, and S. Rafaï, Random walk of a swimmer in a low-reynolds-number medium, Phys. Rev. E **83**, 035301(R) (2011).

[30] D. Qin, Y. Xia, and G. M. Whitesides, Soft lithography for micro- and nanoscale patterning, Nat. Protoc. **5**, 491 (2010).

[31] D. Allan, C. van der Wel, N. Keim, T. A. Caswell, D. Wieker, R. Verweij *et al.*, *Soft-Matter/Trackpy: Trackpy v0.4.2* (Zenodo, 2019).

[32] J. C. Crocker and D. G. Grier, Methods of digital video microscopy for colloidal studies, J. Colloid Interface Sci. **179**, 298 (1996).

[33] M. Martin, A. Barzyk, E. Bertin, P. Peyla, and S. Rafai, Photofocusing: Light and flow of phototactic microswimmer suspension, Phys. Rev. E **93**, 051101(R) (2016).

[34] V. Kantsler, J. Dunkel, M. Polin, and R. E. Goldstein, Ciliary contact interactions dominate surface scattering of swimming eukaryotes, Proc. Natl. Acad. Sci. USA **110**, 1187 (2013).

[35] E. Lushi, V. Kantsler, and R. E. Goldstein, Scattering of biflagellate microswimmers from surfaces, Phys. Rev. E **96**, 023102 (2017).

[36] F. Jan Schwarzendahl and M. G. Mazza, Maximum in density heterogeneities of active swimmers, Soft Matter **14**, 4666 (2018).

[37] M. Contino, E. Lushi, I. Tuval, V. Kantsler, and M. Polin, Microalgae Scatter Off Solid Surfaces by Hydrodynamic and Contact Forces, Phys. Rev. Lett. **115**, 258102 (2015).

[38] K. Drescher, R. E. Goldstein, N. Michel, M. Polin, and I. Tuval, Direct Measurement of the Flow Field Around Swimming Microorganisms, Phys. Rev. Lett. **105**, 168101 (2010).

[39] S. Chen and G. D. Doolen, Lattice Boltzmann method for fluid flows, Annu. Rev. Fluid Mech. **30**, 329 (1998).

[40] M. Brun-Cosme-Bruny, E. Bertin, B. Coasne, P. Peyla, and S. Rafaï, Effective diffusivity of microswimmers in a crowded environment, J. Chem. Phys. **150**, 104901 (2019).

[41] M. E. Cates and J. Tailleur, Europhys. Lett. **101**, 20010 (2013).

[42] J. D. Weeks, D. Chandler, and H. C. Andersen, Role of repulsive forces in determining the equilibrium structure of simple liquids, J. Chem. Phys. **54**, 5237 (1971).

[43] C. K. Aidun and J. R. Clausen, Lattice-boltzmann method for complex flows, Annu. Rev. Fluid Mech. **42**, 439 (2010).

[44] P. L. Bhatnagar, E. P. Gross, and M. Krook, A model for collision processes in gases. I. Small amplitude processes in charged and neutral one-component systems, Phys. Rev. **94**, 511 (1954).

[45] A. J. C. Ladd, Numerical simulations of particulate suspensions via a discretized boltzmann equation. Part 1. Theoretical foundation, J. Fluid Mech. **271**, 285 (1994).

[46] C. S. Peskin, The immersed boundary method, Acta Numer. **11**, 479 (2002).

[47] Z. Guo, C. Zheng, and B. Shi, Discrete lattice effects on the forcing term in the lattice boltzmann method, Phys. Rev. E **65**, 046308 (2002).

[48] C. K. Aidun and Y. Lu, Lattice boltzmann simulation of solid particles suspended in fluid, J. Stat. Phys. **81**, 49 (1995).

[49] C. K. Aidun, Y. Lu, and E.-J. Ding, Direct analysis of particulate suspensions with inertia using the discrete boltzmann equation, J. Fluid Mech. **373**, 287 (1998).

[50] M. E. Cates, K. Stratford, R. Adhikari, P. Stansell, J.-C. Desplat, I. Pagonabarraga, and A. J. Wagner, Simulating colloid hydrodynamics with lattice boltzmann methods, J. Phys. Condens. Matter **16**, S3903 (2004).